

Article

Influence of Severe Plastic Deformation by Extrusion on Microstructure, Deformation and Thermal Behavior under Tension of Magnesium Alloy Mg-2.9Y-1.3Nd

Elena Legostaeva ^{1,*}, Anna Eroshenko ¹, Vladimir Vavilov ², Vladimir A. Skripnyak ³ , Nikita Luginin ^{1,2} , Arsenii Chulkov ², Alexander Kozulin ³ , Vladimir V. Skripnyak ³, Juergen Schmidt ⁴ , Alexey Tolmachev ¹, Pavel Uvarkin ¹ and Yurii Sharkeev ^{1,2} 

- ¹ Institute of Strength Physics and Materials Science, Siberian Branch Russian Academy of Sciences, 634055 Tomsk, Russia; eroshenko@ispms.ru (A.E.); nikishek90@gmail.com (N.L.); tolmach@ispms.ru (A.T.); uvarkin@ispms.ru (P.U.); sharkeev@ispms.ru (Y.S.)
- ² School of Non-Destructive Testing, Research School of High-Energy Physics, National Research Tomsk Polytechnic University, 634050 Tomsk, Russia; vavilov@tpu.ru (V.V.); chulkovao@tpu.ru (A.C.)
- ³ Department of Mechanics of Deformed Solid Body, Faculty of Physics and Engineering, National Research Tomsk State University, 634050 Tomsk, Russia; skrp2006@yandex.ru (V.A.S.); kozulyln@ftf.tsu.ru (A.K.); skrp2012@yandex.ru (V.V.S.)
- ⁴ Department of Electrochemistry, Innovent Technology Development, D-07745 Jena, Germany; js@innovent-jena.de
- * Correspondence: lego@ispms.ru

Abstract: The microstructural investigation, mechanical properties, and accumulation and dissipation of energies of the magnesium alloy Mg-2.9Y-1.3Nd in the recrystallized state and after severe plastic deformation (SPD) by extrusion are presented. The use of SPD provides the formation of a bimodal structure consisting of grains with an average size 15 μm and of ultrafine-grained grains with sizes less than 1 μm and volume fractions up to 50%, as well as of the fine particles of the second Mg_{24}Y_5 phases. It is established that grain refinement during extrusion is accompanied by an increase of the yield strength, increase of the tensile strength by 1.5 times, and increase of the plasticity by 1.8 times, all of which are due to substructural hardening, redistribution of the phase composition, and texture formation. Using infrared thermography, it was revealed that before the destruction of Mg-2.9Y-1.3Nd in the recrystallized state, there is a sharp jump of temperature by 10 $^{\circ}\text{C}$, and the strain hardening coefficient becomes negative and amounts to (−6) GPa. SPD leads to a redistribution of thermal energy over the sample during deformation, does not cause a sharp increase in temperature, and reduces the strain hardening coefficient by 2.5 times.

Keywords: Mg-based bioinert alloys; ultrafine-grained state; severe plastic deformation; microstructure; mechanical properties



Citation: Legostaeva, E.; Eroshenko, A.; Vavilov, V.; Skripnyak, V.A.; Luginin, N.; Chulkov, A.; Kozulin, A.; Skripnyak, V.V.; Schmidt, J.; Tolmachev, A.; et al. Influence of Severe Plastic Deformation by Extrusion on Microstructure, Deformation and Thermal Behavior under Tension of Magnesium Alloy Mg-2.9Y-1.3Nd. *Metals* **2023**, *13*, 988. <https://doi.org/10.3390/met13050988>

Academic Editor: Eric Hug

Received: 31 March 2023

Revised: 28 April 2023

Accepted: 11 May 2023

Published: 19 May 2023



Copyright: © 2023 by the authors. Licensee MDPI, Basel, Switzerland. This article is an open access article distributed under the terms and conditions of the Creative Commons Attribution (CC BY) license (<https://creativecommons.org/licenses/by/4.0/>).

1. Introduction

Recently, there has been an increasing interest in biodegradable metals, which are used in various fields of medicine. Particular attention is attracted to magnesium alloys [1–8] having certain advantages which distinguish them favorably from other materials used in the manufacturing of implants. One of the most important advantages is the ability of magnesium alloys to be resorbed in the human body. This feature makes it possible to avoid surgical operations, which are otherwise needed for removing implants [9,10]. Moreover, magnesium implants demonstrate good biocompatibility and may have antitumor effects. The latter are due to magnesium's ability to release hydrogen during biodegradation, which has a cytopathogenic effect on tumor cells [11,12]. Finally, magnesium alloys have an optimal modulus of elasticity (40–45 GPa), similar to that of the native bone [13,14]. Alloying of magnesium with rare earth metals (RE), such as Y, Nd, Gd, Ce, Dy, etc., leads to

the enhancement of strength characteristics, and to increases in plasticity and corrosion resistance [15–18]. However, in some cases, the achieved level of strength properties does not meet the necessary requirements. This may to some extent limit the use of these materials in implantology.

In view of the above, various deformation methods were proved to be very promising, including severe plastic deformation (SPD), for example, equal-channel angular pressing (ECAP), abc-forging, rotational forging, extrusion, etc. These methods allow one to obtain a high level of mechanical properties in metals by grinding grain to an ultrafine-grained (UFG) state [14–29]. In this case, it becomes possible to significantly improve the mechanical properties of alloys. Of particular importance is that this can be done without additional alloying with elements, which reveal toxic properties and are thus inapplicable, for example, in biomedicine.

Various investigations were conducted to study the microstructure and physico-mechanical properties of the medical materials in which the UFG structure is formed. This applies primarily to studies of ‘pure titanium’ VT1-0, VT1-00, Grade 1, Grade 2, and, to a lesser extent, to titanium and magnesium alloys [30,31]. However, it is worth noting that the use of SPD methods, such as ECAP and abc-forging, does not always lead to the formation of the UFG state in magnesium alloys. As a rule, one obtains a finely dispersed structure with an average grain size of about 1 μm . Therefore, the development of methods and technological regimes of deformation for obtaining the UFG state in magnesium alloys remains an urgent task. In addition, the issues related to obtaining the UFG structure in bulk magnesium alloy samples by SPD are complex and have not yet been fully resolved.

Understanding the mechanisms of plastic deformation and destruction under various types of loading is important for developing new UFG alloys. Strain localization plays a special role, since it determines the features of degradation and destruction of real samples [32–35]. At the same time, the issues related to identification of the mechanisms leading to the destruction of UFG alloys remain poorly understood and require a more detailed analysis.

There are various approaches developed for estimating the criteria of the strength and fracture of materials. One of them is the method of complete diagrams, which makes it possible to find a characteristic for estimating the ultimate damage in the plastic part of the complete tensile diagram after any preloading. The latter has the meaning of the specific work expended for failure. This method also allows one to develop a new criterion for crack resistance [35]. Another approach is based on the evaluation of the accumulation and dissipation of energy during plastic deformation using the method of infrared (IR) thermography.

The IR thermography method [36] has been proved to be very convenient for analyzing the processes in which a material reaches its critical state. This method allows one to analyze the temperature variations of samples throughout the whole range of deformations. It also makes it possible to investigate the evolution of structural defects within materials in real time. As has been shown in Refs. [37–56], despite the absence of external signs of deformation, the shear bands are formed at different stages of deformation. In the same works, it was noted that the accumulation and dissipation of energy develop non-linearly and depend on the loading conditions. It should however be noted that investigations of deformation processes by IR thermography were carried out mainly on steels, aluminum, and titanium alloys in the coarse-grained state [37–56].

In some of our previous works [57–61], comparative studies of the evolution of the temperature distributions, as well as of the peculiarities of energy accumulation and dissipation during the deformation of VT1-0, Zr-1Nb, and Ti-45Nb alloys in the CG and UFG states, were carried out. According to our results, the distribution of the temperature field on the surface of the deformed samples depends on the samples’ structural states, the presence of defective structures, and the mechanical and thermophysical properties of the alloys under study.

The aim of the present work is to study how the extrusion deformation processing of a magnesium alloy of the Mg-Y-Nd system affects the microstructure, mechanical properties, and tensile deformation behavior.

2. Materials and Research Methods

For the present study we used a commercial magnesium Mg-Y-Nd alloy with the following elemental content: Mg-2.9Y-1.3Nd (wt.%): Mg 95.0; Y 2.9; Nd 1.3; Fe \leq 0.2; Al \leq 0.6, manufactured by continuous mold casting [62,63]. In order to refine the grain and thus improve the mechanical properties, the samples were subjected to SPD by extrusion. The alloy billets were deformed by reverse extrusion at a speed of 0.5 mm/s, and the temperature of the billet and the extruder wall was 350 °C. The diameter of the bars was successively reduced from 60 to 14 mm. The accumulated logarithmic degree of deformation as a result of deformation processing of the samples was $e = 1.46$. This parameter was determined as the logarithm of the ratio of the initial to the final thicknesses of the sample at each pressing.

The magnesium alloy was investigated in both the extruded and recrystallized states. The recrystallized state in the Mg-2.9Y-1.3Nd alloy was achieved by annealing at a temperature of 525 °C for 8 h in argon with subsequent cooling in air.

The mechanical tests were performed out on the universal servohydraulic test stand Instron (Instron European Headquarters, High Wycombe, UK). The uniaxial tension of flat samples was conducted at a constant strain rate of 0.01 s^{-1} . To measure the temperature distributions on the surface of the samples, as well as to evaluate the samples' dimensions and shapes including the formation of necks during deformation, we used an infrared radiometric imager FLIR SC 7700M. This allowed obtaining the true deformation $\sigma_{true}(\epsilon_{true})$ and temperature $\Delta T(\epsilon_{true})$ curves, as well as determining the work of plastic deformation $A_p(\epsilon_{true})$, the specific amount of the heat dissipated during deformation (Q), and the energy stored during deformation (E_s). The respective calculation methodology was described elsewhere [57,60].

The true stress σ_{true} was evaluated using the formula:

$$\sigma_{true} = \frac{F(1 + \epsilon_{eng})}{S_0}, \quad (1)$$

where F is the load applied to the sample, S_0 is the initial cross-section area of the sample, $S_0 = a_0 \times b_0$, where a_0 and b_0 are the width and the thickness of the sample, ϵ_{eng} is the engineering deformation, and $\epsilon_{eng} = \frac{\Delta l}{l_0}$ where Δl and l_0 are the elongation and the initial length of the gauge section of the sample, respectively. The true stress in the "neck" zone was calculated as follows:

$$\sigma_{true} = \frac{F}{S_i}, \quad (2)$$

where $S_i = a_i \times b_i$ is the apparent cross-sectional area in the "neck" of the sample corresponding to the i -th IR thermogram and a_i and b_i are the width and the thickness of the sample in the "neck" region for the i -th thermogram. The latter are related by the equation $b_i = b_0 \times a_i/a_0$

The true deformation ϵ_{true} was determined thus:

$$\epsilon_{true} = \ln(1 + \epsilon_{eng}), \quad (3)$$

The total specific work of deformation was estimated using the true strain curves thus:

$$A = \int_0^{\epsilon_{max}} \sigma_{true} d\epsilon_{true}, \quad (4)$$

where ϵ_{max} is the maximum deformation of the sample before fracture.

The work of plastic deformation A_p is defined thus:

$$A_p = A - A_e, \quad (5)$$

where A_e is the work of elastic deformation.

Then, the energy stored during plastic deformation (E_s) can be defined thus:

$$E_s = A_p - Q \quad (6)$$

Using the data obtained by the infrared thermography method, the specific amount of heat released during the deformation process (Q) was estimated by using the obvious formula:

$$Q = c \frac{m}{V} \Delta t. \quad (7)$$

Here, c , m , and V are the specific heat of the sample material, the sample mass, and the sample volume, respectively, and Δt is the average temperature change on the sample surface during its deformation.

The microstructure and phase composition of the samples were studied using the optical microscope AXIOVERT-200MAT (Carl Zeiss, Industrielle Messtechnik GmbH, Oberkochen, Germany), a transmission electron microscope (TEM) (JEOL JEM 2100, JEOL Ltd., Akishima, Tokyo, Japan), and an X-ray diffraction analysis unit using CuK α radiation (Bruker D8 Advance, Karlsruhe, Germany, $\lambda = 1.54 \text{ \AA}$). The measurements were fulfilled in the 2θ range of $10\text{--}90^\circ$, with a scan step of 0.01° and an acquisition time of 1 s. The phase was identified using the cards from the database of the International Center for Diffraction Data (ICDD) PDF4+. To calculate the average size of structural elements (grains, subgrains, fragments) we used the standard secant method [64].

The microhardness was evaluated according to the Vickers on the microhardness tester Duramin 5 (Struers, Ballerup, Denmark). To measure the elastic modulus, we used the nanohardness tester DUH 211S (Shimadzu, Chiyoda-ku, Tokyo, Japan). The modulus value was obtained by pressing the indenter into the sample surface with the simultaneous building up of the 'load-unload' kinetic diagram. The measurements were performed at a load of 200 g. The loading, unloading, and holding time was 10 s. The elastic modulus was calculated by means of graphical derivation of the unloading branch on the diagram [65].

The microstructure of the fracture surface and the texture of the samples were investigated by applying the technique of scanning electron microscopy (SEM) by means of an electron microscope (LEO EVO 50 Carl Zeiss, Oberkochen, Germany) equipped with a backscattered electron diffraction (EBSD).

3. Results and Discussion

Figure 1 shows the microstructure of the Mg-2.9Nd-1.3Y alloy in the recrystallized state. As we can see, the microstructure is uniform over the entire volume of the sample with equiaxed grains of the main α -phase of magnesium (HCP lattice). The average grain size is the same in the longitudinal and in the transverse sections and amounts to $35 \mu\text{m}$ (Figure 1a). The dislocation substructure is represented by individual dislocations and dislocation loops. The dislocation density is low and amounts to only $3 \cdot 10^9 \text{ cm}^{-2}$. In the α -grains of magnesium there are evenly distributed particles of the intermetallic phase (Figure 1b,c) with a high content of yttrium (9–30 wt.%).

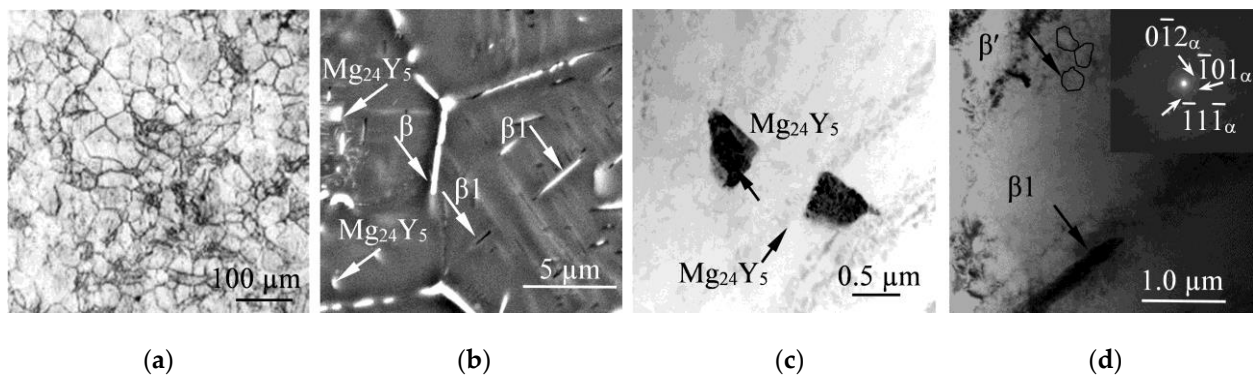


Figure 1. Microstructure of the recrystallized alloy Mg-2.9Nd-1.3Y. (a) Optical image; (b) SEM image; (c,d) Bright-field electron microscopic images with corresponding microdiffraction; (b,c) $Mg_{24}Y_5$ particles; (d) Grid of precipitates of β -phase, precipitates of β' , and β_1 -phase. The arrows show the reflections from the identified phases and the phases themselves.

The intermetallic particles were identified by X-ray microanalysis of the elemental content as $Mg_{24}Y_5$ (BCC lattice). The $Mg_{24}Y_5$ particles, having the form of irregular polyhedrons, were 0.2 to 1 μm in size. Furthermore, the microstructure images show another type of intermetallic phases enriched in Y and Nd, appearing inside or along the grain boundaries. According to [66,67], in the Mg-Y-Nd alloys, these phases are identified as precipitates of intermetallic phases: eutectic equilibrium β -phase ($Mg_{14}Nd_2Y$, FCC lattice), precipitates of the β' -phase ($Mg_{12}NdY$, orthorhombic lattice) of globular morphology, and a plate of the β_1 -phase (Mg_3NdY , FCC lattice). Discharges of the β -phase are localized along the grain boundaries in the form of a grid of up to 0.8–2 μm in thickness (Figure 1b). The average size of the β' -phase ($Mg_{12}YNd$) globules is 0.3 μm and the length and the width of the β_1 -phase plates are within the ranges of 0.3–0.9 μm and 0.02–0.08 μm , respectively.

After extrusion, the refinement of the microstructure occurs in the Mg-2.9Nd-1.3Y alloy. The microstructure has a bimodal character. In the longitudinal section, there are grains 20–25 μm in size, as well as smaller grains 0.5–2 μm in size (Figure 2a). The shapes of most grains are close-to-equiaxed. The fraction of ultrafine-grained grains is about 50%. The average grain sizes for the longitudinal and the cross sections are 14 and 17 μm , respectively. On the TEM images of the microstructure, one observes grain and subgrain boundaries with a clear contrast. These contain an increased density of lattice dislocations in the inner region (Figure 2b). The dislocation density is $4 \cdot 10^{10} \text{ cm}^{-2}$. As in the recrystallized state, the structure (Figure 2b–d) contains particles of $Mg_{24}Y_5$, β -phase ($Mg_{14}Nd_2Y$), precipitates of β' -phase ($Mg_{12}NdY$), globular morphology, and plates of the β_1 -phase (Mg_3NdY).

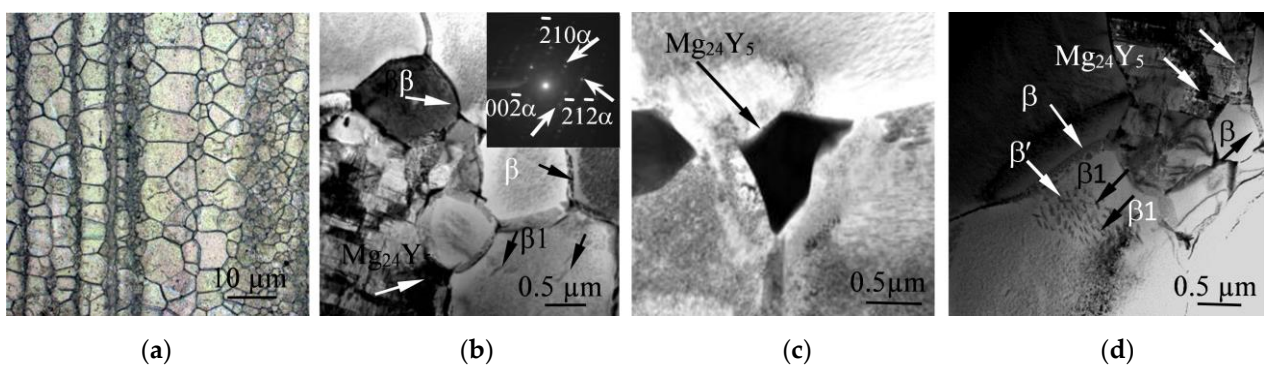


Figure 2. Images of the microstructure of the extruded Mg-2.9Nd-1.3Y alloy: (a) Optical image; (b–d) Bright-field electron microscopic images with corresponding microdiffraction; (b,c) Section of the foil containing particles; (d) Dislocation substructure.

According to the results of the microdiffraction analysis, the $Mg_{24}Y_5$ particles have an increased yttrium content (30 wt.%). Their sizes are in the range 0.3–0.7 μm . The volume fraction of particles of the second $Mg_{24}Y_5$ phase does not exceed 5%. In the extruded alloy, the $Mg_{24}Y_5$ particles are in the form of irregular polyhedrons and are located in the bodies of the grains (Figure 2c). The content of yttrium in the discharge of β -, β' - and β_1 -phases is (9–11) wt.%, and that of neodymium is (4–6) wt.%. The average size of globules of the β' -phase ($Mg_{12}YNd$) is 0.2 μm . The length and the width of the β_1 -phase plates are within the ranges of 0.06–0.3 μm and 0.03–0.04 μm , respectively. Note that the plates of the β_1 -phase are oriented in the same direction. The eutectic β -phase ($Mg_{14}Nd_2Y$) is represented by an irregularly shaped polyhedral and localized along the grain boundaries in the form of a network of precipitates of 0.1–0.3 μm in thickness. In the extruded state, one observes a decrease of the linear dimensions of the particles in the $Mg_{24}Y_5$ intermetallic compounds, as well as of the β -phase and β_1 - and β' -phases.

Figure 3 shows the diffraction patterns for Mg-2.9Nd-1.3Y alloys (a, b) in the recrystallized and the extruded states. For both states, high-intensity reflections from the α -phase of magnesium and low-intensity reflections from the $Mg_{24}Y_5$ intermetallics were found. The intensity of reflections from the intermetallic phases for the recrystallized state is higher than that for the alloy after extrusion. This may indicate a certain increase of the volume fraction of the phases and $Mg_{24}Y_5$ as a result of annealing. For the extruded state of the alloys, redistributions of the reflection intensity (100) and (101) are observed, indicating the reorientation of the grains and formation of a texture. The volume fraction of the secondary phase particles could not be determined by an X-ray diffraction analysis because of their small amount.

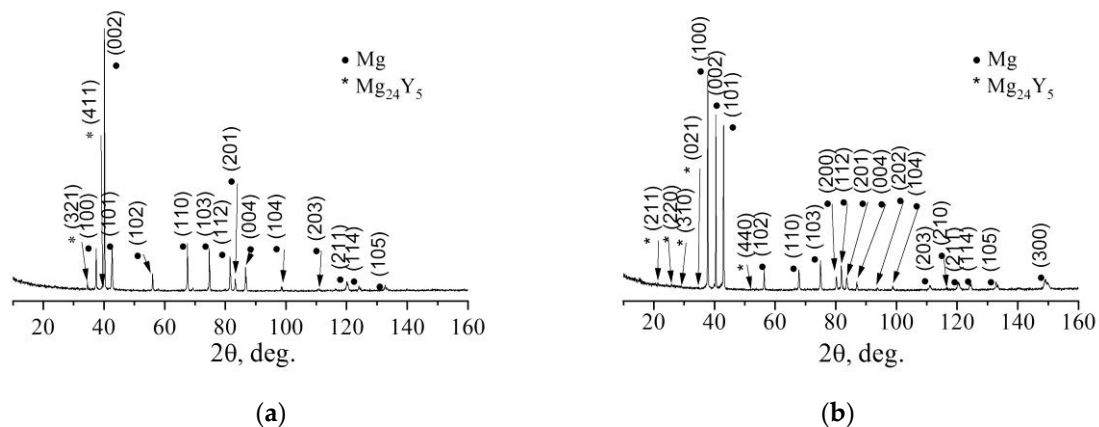


Figure 3. X-ray pattern of magnesium alloy Mg-2.9Nd-1.3: (a) Recrystallized state; (b) Extruded state.

Figure 4 shows EBSD misorientation maps and inverse pole figures for magnesium alloy Mg-2.9Y-1.3Nd in various structural states. On the EBSD maps, the grains are colored according to their crystallographic orientations (the color code is given in the next). On the maps for the two states, one can notice the granular nature of the microstructure. The structure for the extruded state is dominated by a weak crystallographic texture of the $\langle 001 \rangle$ type. The inverse pole figures are presented for different external sections in the crystal: longitudinal X0, transverse Y0, and normal (axial) Z0 in three main planes (0001), (01–10), (11–20). As one can see, in the recrystallized state, the inverse pole figures have clear maxima (Figure 4a), and the maximum reflection density is not concentrated near a particular crystallographic direction. This may point to the formation of an annealing texture [68,69]. After the extrusion of the magnesium alloy, the inverse pole figures become blurred, and the pole density maximum changes its position (Figure 4b). For the main directions of the crystal lattice, high pole densities are observed. The maximum density occurs in the direction $\langle 001 \rangle$ for the longitudinal Y0 and $\langle 010 \rangle$ for the normal Z0 sections. This indicates a pronounced texture. The texture of the extruded magnesium alloy Mg-

Mg-2.9Y-1.3Nd is quite diffuse. Note that the total intensity of the peaks in the extruded state is much higher than that in the case of annealing.

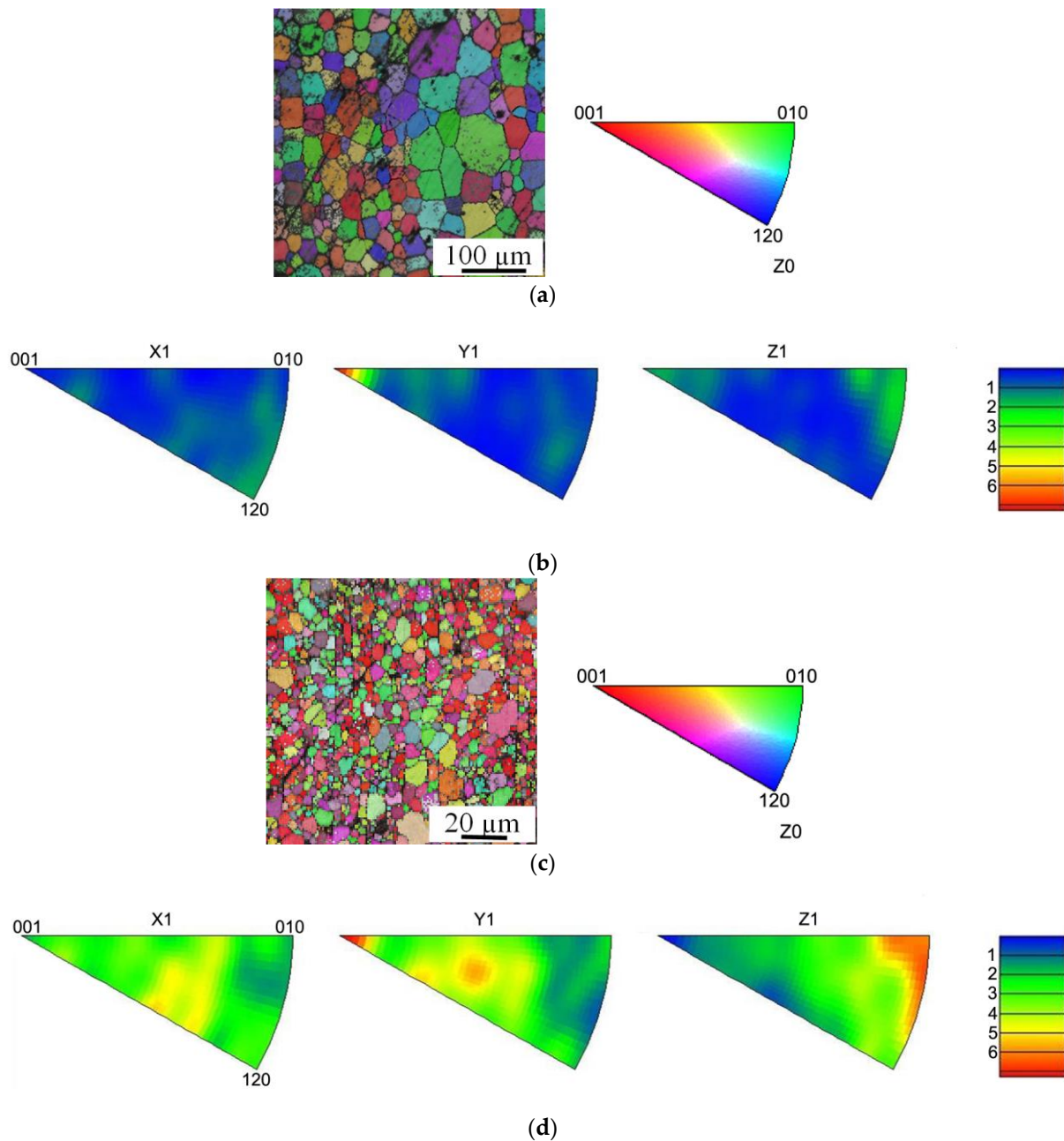


Figure 4. EBSD-images and inverse pole figures of magnesium alloy Mg-2.9Y-1.3Nd: (a,b) Recrystallized state; (c,d) Extruded state. (Half with: 10° , cluster size: 5° , exp. densities (mud): min = 0.02, max = 7.3).

The plasticity of magnesium alloys should be analyzed taking into account the texture factor [70]. The presence of texture changes the activity of the main deformation systems in the basal {0001}, prismatic {1010}, and pyramidal {1122} systems, as well as {1012} twinning. The texture formed after deformation activates the basal and pyramidal sliding, as well as the twinning. At the same time, it hinders the dislocation slide for prismatic planes. On the contrary, the texture for the recrystallized state activates the basal slide and weakens the activity of the prismatic slide. The overall effect of prismatic and pyramidal slide activation is superior to that of the basal slide activation after extrusion. Thus, it can be argued

that the extrusion of an alloy significantly increases both its strength and its plasticity. In addition, the higher relative elongation of the magnesium alloy in the extruded state, compared to in the recrystallized state, can be explained by a slightly lower fraction of second phase particles.

In Figure 5 we demonstrate the conditional engineering curves for Mg-2.9Y-1.3Nd alloy samples in the recrystallized (1) and the extruded (2) states. Using the ‘engineering stress—engineering strain’ diagrams, the following ultimate strength characteristics of Mg-2.9Y-1.3Nd alloys under uniaxial tension conditions can be determined: conditional yield strength σ_{YS} , ultimate strength σ_{UTS} , and maximum plastic deformation before failure ϵ_f . The corresponding values are collected in Table 1. There we also present the microhardness $H\mu$ and the Young’s modulus E for the alloy under study. The results indicate that the grain refinement during extrusion is accompanied by an increase of mechanical properties: the conditional yield strength, tensile strength by 1.5 times, and plasticity by 1.8 times. Moreover, the deformation processing of the Mg-2.9Y-1.3Nd alloy by extrusion leads to an increase in microhardness by a factor of 1.2 and does not cause any significant change in the Young’s modulus of the magnesium alloy (Table 1).

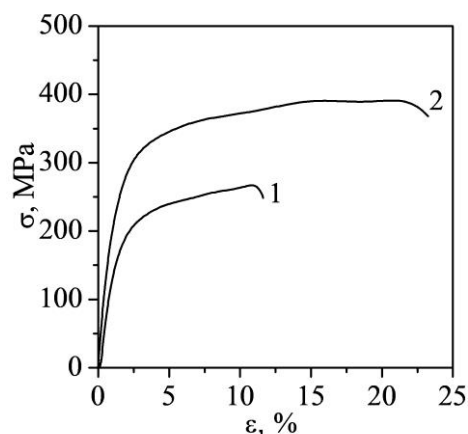


Figure 5. The engineering curves for magnesium alloy Mg-2.9Y-1.3Nd: 1—recrystallized state; 2—extruded state.

Table 1. Mechanical properties of Mg-2.9Y-1.3Nd alloy.

State/Property	σ_{YS} , MPa	σ_{UTS} , MPa	ϵ_f , %	$H\mu$, MPa	E , GPa
Recrystallized state	150 ± 7	230 ± 8	12 ± 1	860 ± 60	33.9 ± 0.5
Extruded state	220 ± 9	340 ± 10	21 ± 1	1210 ± 70	35.0 ± 0.5

The increase in strength is determined by strain hardening associated with the accumulation of dislocation density and by the contribution of the dispersed particles from the second $Mg_{24}Y_5$ phase localized along the grain boundaries. The decrease of strength in the recrystallized state should be assigned to an increase of the grain size and to a decrease of the dislocation density. According to the results of Ref. [70], during deformation at temperatures above 225 °C in the basal slide mechanism in the magnesium alloy, this is realized. In this case, the dislocation slide occurs along the basis planes if these planes are ‘conveniently’ oriented with respect to the direction of the applied stress. In addition, at higher temperatures, the gliding of prismatic and pyramidal systems also becomes possible. This mechanism is preferable for obtaining the optimal combination of the strength and plastic properties of magnesium alloys.

The increase in plasticity after deformation is caused by the activation of an additional mechanism of the dislocation slide, i.e., the slide predominantly along prismatic planes and not along the base planes as in the equilibrium state [71]. The increase of the plasticity strength of the magnesium alloys is associated with the evolution of the dislocation sub-

structure and with the formation of textures as a result of the deformation processing of alloys. This finding agrees with the results obtained by other authors for the magnesium alloys MA2-1 and WE43 after SPD [72,73]. The reason for this may be the formation of a bimodal structure and texture in the Mg-Y-Nd alloy during extrusion, as well as the substructural hardening of the matrix α -phase and redistribution of the phase composition (secondary phases β , β' , and β_1 , and the Mg_{24}Y_5 particles).

Figure 6a,b show the SEM images of the fracture surfaces of the alloy in the extruded and recrystallized states. For the alloy sample after extrusion, on the fracture surface, there are areas of “pitted” microrelief typical of ductile fracture (Figure 6a). The microrelief consists of large “pits” with an average size $20\ \mu\text{m}$ and a heteroaxial shape and smaller pits with an average size of less than $5\ \mu\text{m}$.

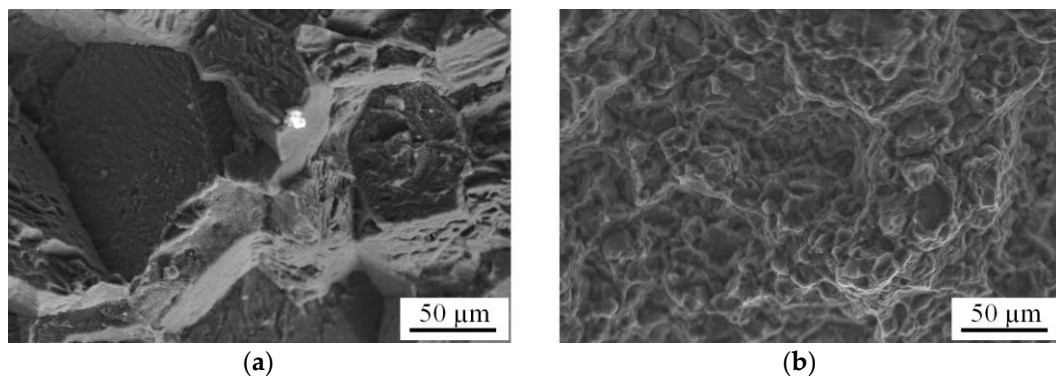


Figure 6. SEM- images of the fracture surface of Mg-2.9Y-1.3Nd magnesium alloy samples: (a) Recrystallized state; (b) Extruded state.

The fracture surface of the alloy after extrusion has a uniform structure, and this may indicate the macroplastic nature of the fracture. The fracture surface of the sample for the recrystallized state has a “rough” faceted structure (Figure 6b). The fracture microrelief consists mainly of large smooth and flat fragments of $30\text{--}100\ \mu\text{m}$ in size. There are protrusions and chips at the boundaries of the fragments. Note that there are areas of pit fracture between the flat fragments. The brittle nature of the fracture is evidenced by the presence of chips and protrusions of the facets. The presence of flat facets with characteristic flow lines is typical of brittle fracture. For both states, there are pores that appeared during the plastic deformation.

Figure 7 shows the true deformation curves $\sigma_{true}(\epsilon_{true})$ and the corresponding dependences of the strain hardening coefficient $\theta(\epsilon_{true}) = d\sigma_{true}/d\epsilon_{true}$ for the Mg-2.9Y-1.3Nd alloy in the recrystallized (1) and the extruded (2) states. In the recrystallized state, several stages of deformation can be distinguished: transitional stage (T), stage III, stage IV, stage V, and stage VII (according to the classification used in [74,75]).

Although a decrease of θ is observed at the transitional stage T, the shape of the curve is not parabolic (Figure 6). Stage II with a constant θ is suppressed, and it is immediately followed by stage III up to $\epsilon_{true} \sim 0.03$, at which θ decreases and the dependence $\sigma = f(\epsilon)$ becomes parabolic. The next stage IV ($0.03 < \epsilon_{true} < 0.1$) is almost linear. At a short parabolic stage V ($0.1 < \epsilon_{true} < 0.105$), the strain hardening coefficient drops sharply to almost zero. Finally, at the final stage, stage VII ($0.105 < \epsilon_{true} < 0.115$), a sharp drop of θ to (-6) GPa is observed, and the alloy is destroyed.

A similar trend may be observed on the temperature curve $\Delta T(\epsilon_{true})$ in Figure 8. In their case, for the Mg-2.9Y-1.3Nd alloy in the recrystallized state, there is an extended part of the curve (up to $\epsilon_{true} \sim 0.03$, corresponds to the stage III on the deformation curves) on which the temperature decreases by about $0.5\ ^\circ\text{C}$ and becomes negative. This is due to the well-known thermoelastic effect [76].

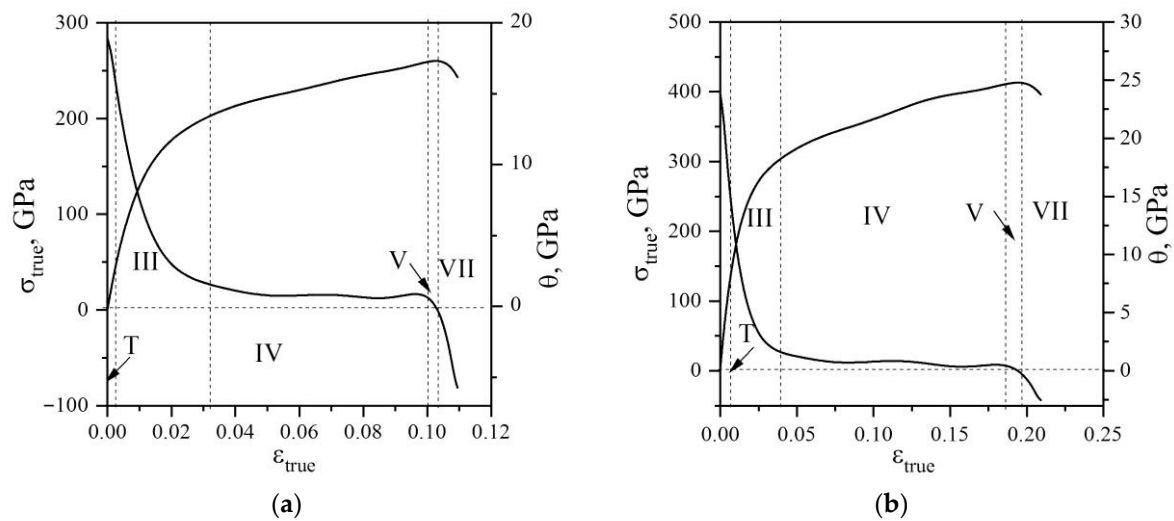


Figure 7. True deformation curves $\sigma_{true}(\epsilon_{true})$ and the corresponding dependences of the strain hardening coefficient $\theta(\epsilon_{true})$ for Mg 2.9Y-1.3Nd alloy samples: (a) Recrystallized state; (b) Extruded state.

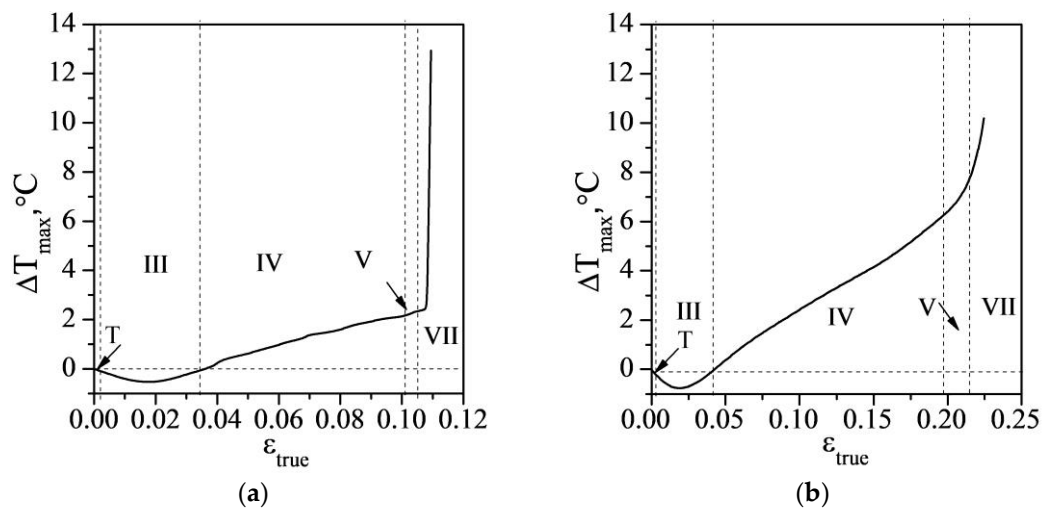


Figure 8. Temperature curves $\Delta T(\epsilon_{true})$ for Mg-2.9Y-1.3Nd alloy samples: (a) Recrystallized state; (b) Extruded state.

At the next stage, stage IV ($0.03 < \epsilon_{true} < 0.1$) the temperature increases by about $2.5\text{ }^{\circ}\text{C}$, followed by a very short stage V ($0.1 < \epsilon_{true} < 0.105$). Finally, at the final stage, stage VII ($0.105 < \epsilon_{true} < 0.115$), there is a sharp jump by $10\text{ }^{\circ}\text{C}$ followed by the destruction of the alloy.

On the curves $\sigma_{true}(\epsilon_{true})$ and $\theta(\epsilon_{true})$ for the Mg-2.9Y-1.3Nd alloy in the extruded state, the following deformation stages can be isolated: transitional stage (T) with θ increasing to $\epsilon_{true} < 0.002$, parabolic stage III with decreasing θ ($0.01 < \epsilon_{true} < 0.04$), linear stage IV with almost constant θ ($0.04 < \epsilon_{true} < 0.19$), parabolic stage V with decreasing θ ($0.19 < \epsilon_{true} < 0.2$), and stage VII with negative θ ($0.2 < \epsilon_{true} < 0.225$).

On the curves depicting the temperature for the Mg-2.9Y-1.3Nd alloy in the extruded state, the part corresponding to a negative temperature (stage III on the deformation curves) increases to $\epsilon_{true} \sim 0.04$. Then, at stages IV and V ($0.04 < \epsilon_{true} < 0.2$), an increase in ΔT by about $5\text{ }^{\circ}\text{C}$ is observed. In contrast to what has been noted in the recrystallized state, before the destruction of the extruded Mg-2.9Y-1.3Nd alloy, at stage VII there is no sharp increase in temperature; ΔT increases only by about $2\text{ }^{\circ}\text{C}$. The strain hardening coefficient decreases by 2.5 and reaches a value (-1.5) GPa.

Figure 9 shows a series of frames from thermal films for the Mg-2.9Y-1.3Nd alloy in the recrystallized (a) and the extruded (b) states. The shape of the IR thermograms indicates that during the deformation of the recrystallized sample, the plastic deformation bands, which are sources of heat release, are less pronounced, and a thermal effect manifests itself insignificantly until the destruction of the sample (Figure 9a). Just before the destruction, one observes a small area of localized deformation whose appearance determines the locations of the defects. Then, in this region, two deformation bands, directed at an angle of 45° , intersect, a sharp jump of temperature is observed, and the instantaneous destruction of the sample occurs.

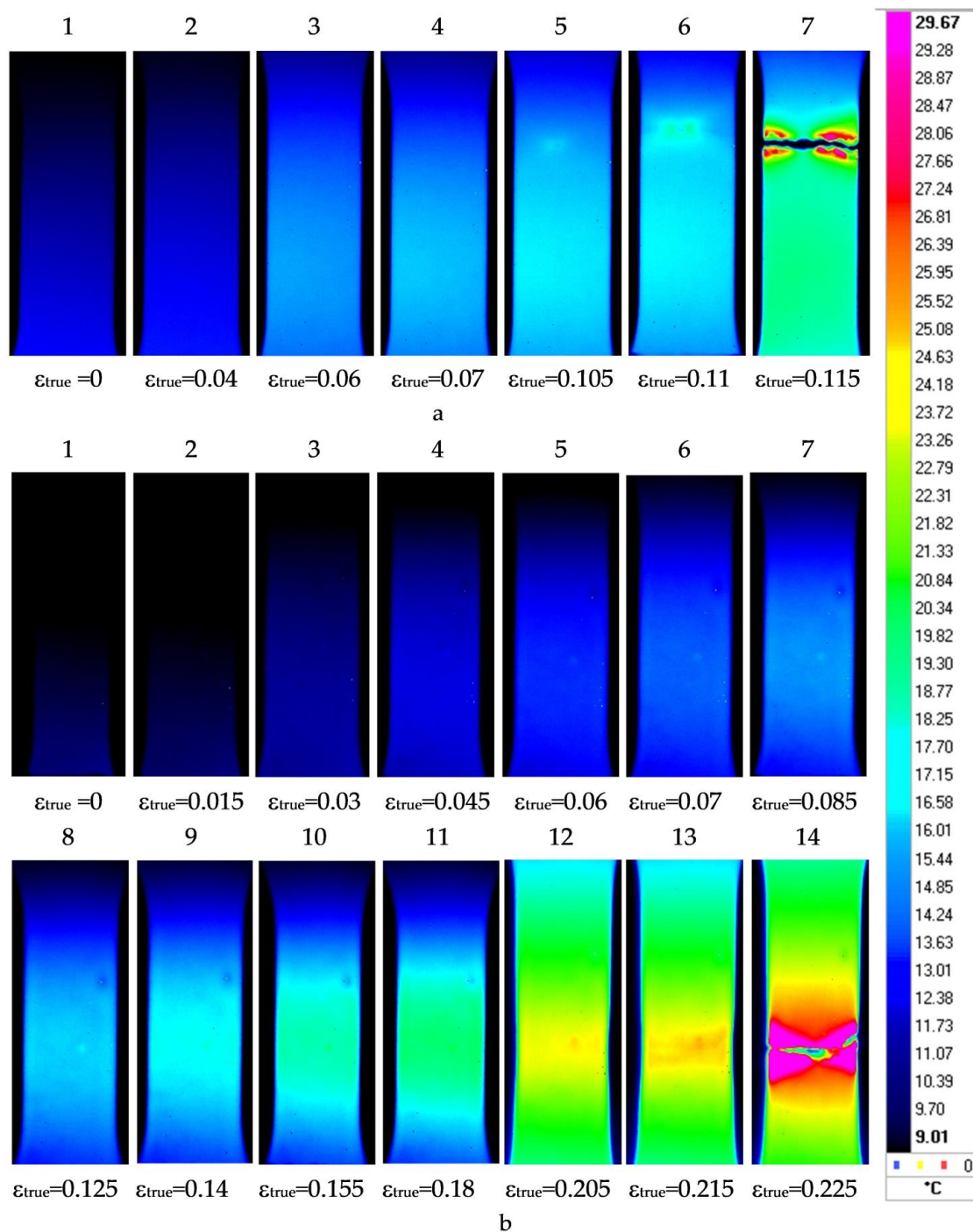


Figure 9. Thermograms of a deformed sample of Mg-2.9Y-1.3Nd alloy, $T_0 = 23^\circ\text{C}$: (a) Recrystallized state; (b) Extruded state.

In an extruded sample with deformations above $\varepsilon_{\text{true}} = 0.085$, plastic deformation bands can be observed whose direction corresponds to the highest shear stresses. In the deformation lines, the alloy is in a plastically activated state, while other regions of the alloy operate in the elastic deformation area. As the flow stress increases, the width of the deformation bands increases, and this is accompanied by a gradual increase of temperature and by the generation of the deformation centers, which increase in size, unite, and develop in the form of a main line.

Further deformation, maximum temperature increase, and destruction of the alloy occur in this region, in which the main line is generated without the formation of a 'neck' (Figure 9b).

In Figure 10 the energy parameters, namely the specific work of plastic deformation A_p , the amount of released heat Q , and absorbed energy during plastic deformation E_s , are plotted as functions of the true strain released during deformation for the Mg-2.9Y-1.3Nd alloy in the recrystallized (a) and the extruded (b) states.

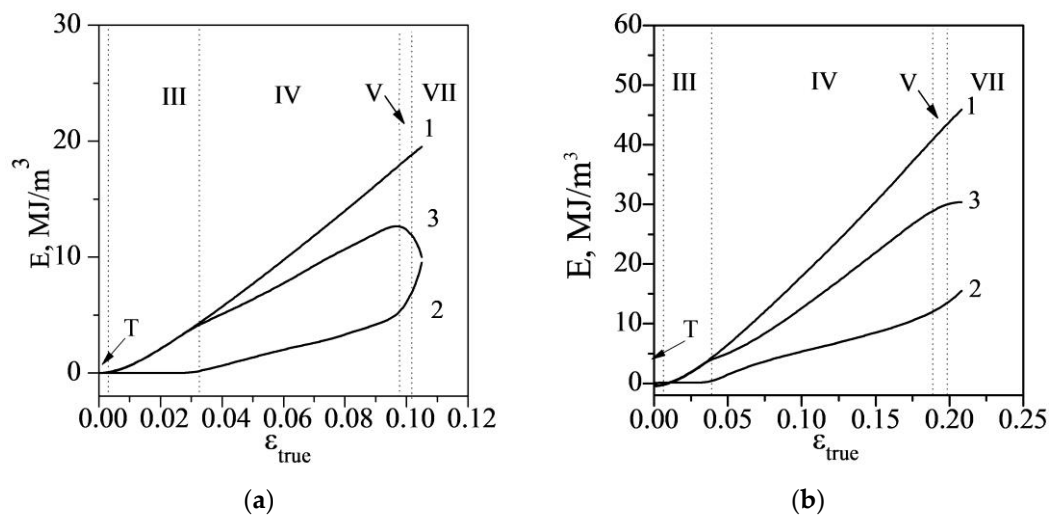


Figure 10. Dissipation and accumulation of energy during plastic deformation of magnesium alloy Mg-2.9Y-1.3Nd: (a) Recrystallized state; (b) Extruded state. 1—work of plastic deformation (A_p), 2—specific amount of heat released during deformation (Q), 3—energy absorbed during the plastic deformation (E_s).

The limiting values of the specific work of plastic deformation were 20 MJ/m^3 and 45 MJ/m^3 for the Mg-2.9Y-1.3Nd alloy in the recrystallized and extruded states, respectively.

From the dependences shown in the figure, one can conclude that for the Mg-2.9Y-1.3Nd alloy samples, in both the extruded and the recrystallized states, the amount of heat released during deformation is different in different areas. At the initial stage, up to $\varepsilon_{\text{true}} \sim 0.03$, almost 100% of the work of plastic deformation is converted into internal energy. This indicates the ability of the alloy to effectively use the structural energy absorption channel at the initial stage of deformation, regardless of its structural state, and this is associated with dispersion strengthening by intermetallic particles.

Then, the dependences of the released and the absorbed energy in the recrystallized and extruded states behave linearly. For the samples in the recrystallized state, the amount of the heat released due to the thermoplastic effect comprises 60% of the work of plastic deformation, and comprises to 12 MJ/m^3 , whereas the specific energy absorbed by the alloy is about 40% of the work of plastic deformation and is equal to 8 MJ/m^3 . In this case, for the alloy in the recrystallized state, before fracture, a sharp temperature jump of $10 \text{ }^\circ\text{C}$ occurs, and the strain hardening coefficient becomes negative, amounting to $(-6) \text{ GPa}$, indicating a local softening of the alloy.

At the same time, the amount of heat released due to the thermoplastic effect in the extruded state is about 35% of the work of plastic deformation (15 MJ/m^3), and the remaining 65% of the energy (30 MJ/m^3) is absorbed by the alloy. This points to the fact that the magnesium alloy in the extruded state dissipates energy twice as efficiently as it does in the recrystallized state.

Obviously, the amount of released heat depends on the structural and phase state as well as on the thermophysical properties of the materials. Previously, it was shown that the amount of heat released from the total strain energy for coarse-grained (CG) titanium was 50% [77], for annealed stainless steel 60–70% [78,79], and for copper 80–90% [80].

The formation of the UFG state also has a strong effect on energy dissipation. In [77], it was shown that substructural hardening in UFG pure titanium under SPD leads to changes in deformation, thermal behavior, and energy accumulation and dissipation during deformation. At the initial stage, up to $\varepsilon_{\text{true}} \sim 0.04$, almost the whole energy of plastic deformation is stored by the material. In the next stages, the amount of released heat increases and reaches 70% just before destruction, whereas the energy stored by the material comprises 30% of the work of plastic deformation. The dispersion strengthening by the ω -phase particles and the α -phase formation in the UFG Ti-45Nb alloy reduce the influence of the UFG structure on the deformation and on thermal behavior, especially at the initial stage of deformation. At this stage, up to $\varepsilon_{\text{true}} \sim 0.05$, almost the total energy of plastic deformation is stored by Ti-45Nb in both the CG and the UFG states. In the next stages, the amount of released heat increases and reaches 40% and 70% just before destruction, whereas the amounts of energy absorbed by the material are 60% and 30% of the work of plastic deformation, respectively, for the Ti-45Nb alloy in the CG and UFG states.

Moreover, our data are in good agreement with the results of [47], where the simulation of energy accumulation, and its dissipation during plastic deformation, was performed. It was shown in [47] that the UFG state of metals contributes to the accumulation of the energy of plastic deformation at the initial stage of deformation. At the same time, dispersion strengthening and the presence of strengthening particles in alloys weaken the effect of substructural hardening during the formation of the UFG structure, as has been demonstrated by the results of the present work.

Thus, SPD by extrusion of the magnesium alloy Mg-2.9Y-1.3Nd leads to formation of a bimodal structure consisting of grains with an average size of $15 \mu\text{m}$ and ultrafine-grained grains (less than $1 \mu\text{m}$ in size) with a volume fraction of up to 50 %, as well as fine particles of the second phases Mg_{24}Y_5 and equilibrium β -phase and metastable β_1 - and β' -phases and texture formation. It provides a significant increase of mechanical properties and affects the deformation behavior and regularities of energy accumulation and dissipation during tension.

4. Conclusions

A comprehensive analysis of the microstructure and deformation, as well as the corresponding temperature dependences, demonstrate the significant influence of the extrusion on the regularities of energy accumulation and dissipation during plastic deformation of the Mg-2.9Y-1.3Nd alloy.

It is shown that the use of SPD by the extrusion method in the magnesium alloy Mg-2.9Y-1.3Nd promotes the formation of the UFG state (the fraction of UFG grains is 50% of the volume), as well as the occurrence of fine particles of the second phases of Mg_{24}Y_5 and equilibrium β -phase, metastable β_1 - and β' -phases, and the formation of texture.

It was found that the refinement of the SPD structure by extrusion of Mg-2.9Y-1.3Nd leads to an increase in the yield strength, increase in the tensile strength by 1.5 times, and increase in the ductility by 1.8 times due to substructural strengthening, redistribution of the phase composition, and texture formation.

It was revealed that SPD leads to the redistribution of thermal energy over the sample during deformation, does not cause a sharp increase in temperature, and reduces the

strain hardening coefficient by a factor of 2.5. The magnesium alloy in the extruded state dissipates energy twice as efficiently as it does in the recrystallized state.

Author Contributions: Conceptualization, V.V., V.A.S., J.S. and Y.S.; methodology, E.L., A.E., V.V., V.A.S. and Y.S.; investigation, E.L., A.E., A.C., N.L., A.K., V.V.S., A.T., P.U. and J.S.; resources E.L., A.E., A.C. and A.K.; software—A.C., A.K., N.L. and V.V.S.; writing—original draft preparation, E.L., A.E. and Y.S.; writing—review and editing, E.L. and A.E.; visualization E.L. and A.E., supervision V.V., V.A.S. and Y.S. All authors have read and agreed to the published version of the manuscript.

Funding: The work was performed according to the Government Research Assignment for the Institute of Strength Physics and Materials Science of the Siberian Branch of the Russian Academy of Sciences (ISPMS SB RAS), project No. FWRW-2021-0004 and methodologically supported by the Tomsk Polytechnic University Development Program (grant Priority 2030-NIP-EB-008-0000-2023).

Data Availability Statement: Not applicable.

Acknowledgments: Experimental research was conducted using the equipment of the Common Use Center “Nanotech” at the Institute of Strength, Physics, and Materials Science, SB RAS (ISPMS SB RAS, Tomsk, Russia).

Conflicts of Interest: The authors declare that they have no known competing financial interest or personal relationships that could have appeared to influence the work reported in this paper.

References

1. Liu, C.; Ren, Z.; Xu, Y.; Pang, S.; Zhao, X.; Zhao, Y. Biodegradable Magnesium Alloys Developed as Bone Repair Materials: A Review. *Scanning* **2018**, *2018*, 9216314. [[CrossRef](#)] [[PubMed](#)]
2. Tsakiris, V.; Tardei, C.; Clicinschi, F.M. Biodegradable Mg alloys for orthopedic implants—A review. *J. Magnes. Alloy.* **2021**, *9*, 1884–1905. [[CrossRef](#)]
3. Bazhenov, V.; Kolytgin, A.; Komissarov, A.; Li, A.; Bautin, V.A.; Khasenova, R.; Anishchenko, A.; Seferyan, A.; Komissarova, J.; Estrin, Y. Gallium-containing magnesium alloy for potential use as temporary implants in osteosynthesis. *J. Magnes. Alloy.* **2020**, *8*, 352–363. [[CrossRef](#)]
4. He, M.; Chen, L.; Yin, M.; Xu, S.; Liang, Z. Review on magnesium and magnesium-based alloys as biomaterials for bone immobilization. *J. Mater. Res. Technol.* **2023**, *23*, 4396–4419. [[CrossRef](#)]
5. Papenberg, N.P.; Gneiger, S.; Weißensteiner, I.; Uggowitz, P.J.; Pogatscher, S. Mg-alloys for forging applications—A review. *Materials* **2020**, *13*, 985. [[CrossRef](#)]
6. Wang, J.; Dou, J.; Wang, Z.; Hu, C.; Yu, H.; Chen, C. Research progress of biodegradable magnesium-based biomedical materials: A review. *J. Alloys Compd.* **2022**, *923*, 66377. [[CrossRef](#)]
7. Chen, J.; Tan, L.; Yu, X.; Etim, I.P.; Ibrahim, M.; Yang, K. Mechanical properties of magnesium alloys for medical application: A review. *J. Mech. Behav. Biomed. Mater.* **2018**, *87*, 68–79. [[CrossRef](#)]
8. Xie, J.; Wang, L.; Zhang, J.; Lu, L.; Zhang, Z.; He, Y.; Wu, R. Developing new Mg alloy as potential bone repair material via constructing weak anode nano-lamellar structure. *J. Magnes. Alloy.* **2023**, *11*, 154–175. [[CrossRef](#)]
9. Witte, F.; Hort, N.; Vogt, C.; Cohen, S.; Kainer, K.U.; Willumeit, R.; Feyerabend, F. Degradable biomaterials based on magnesium corrosion. *Curr. Opin. Solid State Mater. Sci.* **2008**, *12*, 63–72. [[CrossRef](#)]
10. Li, X.; Liu, X.; Wu, S.; Yeung, K.; Zheng, Y.; Chu, P.K. Design of magnesium alloys with controllable degradation for biomedical implants: From bulk to surface. *Acta Biomater.* **2016**, *45*, 2–30. [[CrossRef](#)]
11. Chen, Y.; Xiao, M.; Zhao, H.; Yang, B. On the antitumor properties of biomedical magnesium metal. *J. Mater. Chem. B* **2014**, *3*, 849–858. [[CrossRef](#)] [[PubMed](#)]
12. Agha, N.A.; Liu, Z.; Feyerabend, F.; Willumeit, R.; Gasharova, B.; Heidrich, S.; Mihailova, B. The effect of osteoblasts on the surface oxidation processes of biodegradable Mg and Mg-Ag alloys studied by synchrotron IR microspectroscopy. *Mater. Sci. Eng. C* **2018**, *91*, 659–668. [[CrossRef](#)] [[PubMed](#)]
13. Sun, J.; Xu, B.; Yang, Z.; Zhuo, X.; Han, J.; Wu, Y.; Song, D.; Liu, H.; Jiang, J.; Ma, A. Developing an industrial-scale ECAP Mg-Al-Zn alloy with multi-heterostructure for synchronously high strength and good ductility. *Mater. Charact.* **2020**, *164*, 110341. [[CrossRef](#)]
14. Yao, H.; Zha, X.; Xiong, Y.; Wang, S.; Huttula, M.; Cao, W. Stress corrosion cracking behavior of an as-extruded Mg-1.8Zn-0.5Zr-1.5Gd magnesium alloy in a simulated body fluid. *Kov. Mater.-Met. Mater.* **2022**, *60*, 327–340. [[CrossRef](#)]
15. Fu, W.; Wang, R.; Wu, K.; Kuang, J.; Zhang, J.; Liu, G.; Sun, J. The influences of multiscale second-phase particles on strength and ductility of cast Mg alloys. *J. Mater. Sci.* **2019**, *54*, 2628–2647. [[CrossRef](#)]
16. Zhou, Y.L.; Li, Y.; Luo, D.M.; Ding, Y.; Hodgson, P. Microstructures, mechanical and corrosion properties and biocompatibility of as extruded Mg-Mn-Zn-Nd alloys for biomedical applications. *Mater. Sci. Eng. C* **2015**, *49*, 93–100. [[CrossRef](#)]
17. Yao, H.; Wen, J.; Xiong, Y.; Liu, Y.; Lu, Y.; Cao, W. Microstructures, mechanical properties, and corrosion behavior of As-Cast Mg-2.0Zn-0.5Zr-xGd (wt %) biodegradable alloys. *Materials* **2018**, *11*, 1564. [[CrossRef](#)]

18. Ren, L.; Li, B.; Chen, Z.; Gao, S.; Quan, Y.; Qian, L. Interfacial Microstructure Analysis of AZ31 Magnesium Alloy during Plastic Deformation Bonding. *Processes* **2021**, *9*, 1857. [[CrossRef](#)]
19. Vaughan, M.; Karayan, A.; Srivastava, A.; Mansoor, B.; Seitz, J.; Eifler, R.; Karaman, I.; Castaneda, H.; Maier, H. The effects of severe plastic deformation on the mechanical and corrosion characteristics of a bioresorbable Mg-ZKQX6000 alloy. *Mater. Sci. Eng. C* **2020**, *115*, 111130. [[CrossRef](#)]
20. Yuan, Y.; Ma, A.; Gou, X.; Jiang, J.; Arhin, G.; Song, D.; Liu, H. Effect of heat treatment and deformation temperature on the mechanical properties of ECAP processed ZK60 magnesium alloy. *Mater. Sci. Eng. A* **2016**, *677*, 125–132. [[CrossRef](#)]
21. Alateyah, A.I.; El-Garaihy, W.H.; Alawad, M.O.; El Sanabary, S.; Elkhatatny, S.; Dahish, H.A.; Kouta, H. The Effect of ECAP Processing Conditions on Microstructural Evolution and Mechanical Properties of Pure Magnesium—Experimental, Mathematical Empirical and Response Surface Approach. *Materials* **2022**, *15*, 5312. [[CrossRef](#)] [[PubMed](#)]
22. Bednarczyk, I.; Kuc, D. The Influence of the Deformation Method on the Microstructure and Properties of Magnesium Alloy Mg-Y-RE-Zr. *Materials* **2022**, *15*, 2017. [[CrossRef](#)] [[PubMed](#)]
23. Pan, H.; Yang, C.; Yang, Y.; Dai, Y.; Zhou, D.; Chai, L.; Huang, Q.; Yang, Q.; Liu, S.; Ren, Y.; et al. Ultra-fine grain size and exceptionally high strength in dilute Mg–Ca alloys achieved by conventional one-step extrusion. *Mater. Lett.* **2018**, *237*, 65–68. [[CrossRef](#)]
24. Tong, L.; Chu, J.; Jiang, Z.; Kamado, S.; Zheng, M. Ultra-fine grained Mg-Zn-Ca-Mn alloy with simultaneously improved strength and ductility processed by equal channel angular pressing. *J. Alloys Compd.* **2019**, *785*, 410–421. [[CrossRef](#)]
25. Minárik, P.; Král, R.; Pešička, J.; Chmelík, F. Evolution of mechanical properties of LAE442 magnesium alloy processed by extrusion and ECAP. *J. Mater. Res. Technol.* **2015**, *4*, 75–78. [[CrossRef](#)]
26. Merson, D.; Brilevsky, A.; Myagkikh, P.; Markushev, M.; Vinogradov, A. Effect of deformation processing of the dilute Mg-1Zn-0.2Ca alloy on the mechanical properties and corrosion rate in a simulated body fluid. *Lett. Mater.* **2020**, *10*, 217–222. [[CrossRef](#)]
27. Long, J.; Xiao, G.; Xia, Q.; Wang, X. Study of microstructure evolution of magnesium alloy cylindrical part with longitudinal inner ribs during hot flow forming by coupling ANN-modified CA and FEA. *J. Magnes. Alloy.* **2022**, *in press*. [[CrossRef](#)]
28. Torkian, A.; Faraji, G.; Karimpour, M. Mechanical Properties and Microstructure of WE43 Mg Alloy Processed by Warm ECAP Followed by Extrusion. *Arch. Metall. Mater.* **2018**, *63*, 1093–1100. [[CrossRef](#)]
29. Dvorský, D.; Kubásek, J.; Hosová, K.; Čavojský, M.; Vojtěch, D. Microstructure, Mechanical, Corrosion, and Ignition Properties of WE43 Alloy Prepared by Different Processes. *Metals* **2021**, *11*, 728. [[CrossRef](#)]
30. Valiev, R.Z.; Zhilyaev, A.P.; Langdon, T.G. *Bulk Nanostructured Materials: Fundamentals and Applications*; John Wiley & Sons, Inc.: Hoboken, NJ, USA, 2013; 456p. [[CrossRef](#)]
31. Sharkeev, Y.; Eroshenko, A.; Legostaeva, E.; Kovalevskaya, Z.; Belyavskaya, O.; Khimich, M.; Epple, M.; Prymak, O.; Sokolova, V.; Zhu, Q.; et al. Development of Ultrafine-Grained and Nanostructured Bioinert Alloys Based on Titanium, Zirconium and Niobium and Their Microstructure, Mechanical and Biological Properties. *Metals* **2022**, *12*, 1136. [[CrossRef](#)]
32. Walley, S.M. Shear localization: A historical overview. *Metall. Mater. Trans. A* **2007**, *38A*, 2007–2629. [[CrossRef](#)]
33. Chichili, D.R.; Ramesh, K.; Hemker, K.J. Adiabatic shear localization in α -titanium: Experiments, modeling and microstructural evolution. *J. Mech. Phys. Solids* **2004**, *52*, 1889–1909. [[CrossRef](#)]
34. Xu, Y.; Zhang, J.; Bai, Y.; Meyers, M. Shear Localization in Dynamic Deformation: Microstructural Evolution. *Met. Mater. Trans. A* **2008**, *39*, 811–843. [[CrossRef](#)]
35. Chausov, M.; Maruschak, P.; Hutsaylyuk, V.; Śniezek, L.; Pylypenko, A. Effect of complex combined loading mode on the fracture toughness of titanium alloys. *Vacuum* **2018**, *147*, 51–57. [[CrossRef](#)]
36. Vavilov, V. Thermal NDT: Historical milestones, state-of-the-art and trends. *Quant. Infrared Thermogr. J.* **2014**, *11*, 66–83. [[CrossRef](#)]
37. Oliferuk, W.; Maj, M.; Zembrzycki, K. Determination of the Energy Storage Rate Distribution in the Area of Strain Localization Using Infrared and Visible Imaging. *Exp. Mech.* **2013**, *55*, 753–760. [[CrossRef](#)]
38. Oliferuk, W.; Kochanowski, K. Analysis of the modified impulse method for determining the thermal diffusivity of materials. *SSRN Electron. J.* **2022**. [[CrossRef](#)]
39. Plekhov, O.A.; Uvarov, S.V.; Naimark, O.B.; Saintier, N.; Palin-Luc, T. Theoretical analysis, infrared and structural investigation of dissipation energy in metals under cyclic loading. *Mater. Sci. Eng. A* **2007**, *462*, 367–369. [[CrossRef](#)]
40. Bagavathiappan, S.; Lahiri, B.; Saravanan, T.; Philip, J.; Jayakumar, T. Infrared thermography for condition monitoring—A review. *Infrared Phys. Technol.* **2013**, *60*, 35–55. [[CrossRef](#)]
41. Meola, C.; Carlomagno, G.M. Recent advances in the use of infrared thermography. *Meas. Sci. Technol.* **2004**, *15*, R27–R58. [[CrossRef](#)]
42. Pieczyńska, E.A.; Maj, M.; Golasiński, K.; Staszczak, M.; Furuta, T.; Kuramoto, S. Thermomechanical Studies of Yielding and Strain Localization Phenomena of Gum Metal under Tension. *Materials* **2018**, *11*, 567. [[CrossRef](#)] [[PubMed](#)]
43. Golasiński, K.M.; Staszczak, M.; Pieczyńska, E.A. Energy Storage and Dissipation in Consecutive Tensile Load-Unload Cycles of Gum Metal. *Materials* **2023**, *16*, 3288. [[CrossRef](#)] [[PubMed](#)]
44. Plekhov, O.; Chudinov, V.; Leont'ev, V.; Naimark, O. Experimental investigations of the laws of energy dissipation during dynamic deformation of nanocrystalline titanium. *Tech. Phys. Lett.* **2009**, *35*, 92–95. [[CrossRef](#)]
45. Vshivkov, A.; Iziumova, A.; Prokhorov, A.; Mybassarova, V.; Plekhov, O. Approximation of Heat Dissipation-Crack Rate Curve for Fatigue Crack in Stainless Steel. *J. Phys. Conf. Ser.* **2021**, *1945*, 012063. [[CrossRef](#)]

46. Naimark, O.B.; Sharkeev, Y.P.; Mairambekova, A.M.; Bannikov, M.V.; Eroshenko, A.Y.; Vedernikova, A.I. Failure mechanisms of titanium VT1–0 and zirconium alloy E110 in ultrafine-grained, fine-grained and coarse-grained states under cyclic loading in gigacycle regime. *Lett. Mater.* **2018**, *8*, 317–322. (In Russian) [[CrossRef](#)]
47. Plekhov, O.; Panteleev, I.; Naimark, O. Energy accumulation and dissipation in metals as a result of structural-scaling transitions in a mesodefekt ensemble. *Phys. Mesomech.* **2007**, *10*, 294–301. [[CrossRef](#)]
48. Naimark, O.; Palin-Luc, T. Gigacycle fatigue: Non-local and scaling aspects of damage localization, crack initiation and propagation. *Procedia Struct. Integr.* **2016**, *2*, 1143–1148. [[CrossRef](#)]
49. Mairambekova, A.M.; Eroshenko, A.Y.; Oborin, V.A.; Bannikov, M.V.; Chebodaeva, V.V.; Terekhina, A.I.; Naimark, O.B.; Dmitriev, A.I.; Sharkeev, Y.P. Characteristic Features of Ultrafine-Grained Ti-45 wt.% Nb Alloy under High Cycle Fatigue. *Materials* **2021**, *14*, 5365. [[CrossRef](#)]
50. Moyseychik, E.A.; Vavilov, V.P. Analyzing patterns of heat generated by the tensile loading of steel rods containing discontinuity-like defects. *Int. J. Damage Mech.* **2017**, *27*, 950–960. [[CrossRef](#)]
51. Moyseychik, E.; Vavilov, V.; Kuimova, M. Infrared thermographic assessment of heat release phenomena in steel parts subjected to quasi-static deformation. *Measurement* **2021**, *185*, 110117. [[CrossRef](#)]
52. Zhang, H.; Wu, G.; Yan, Z.; Guo, S.; Chen, P.; Wang, W. An experimental analysis of fatigue behavior of AZ31B magnesium alloy welded joint based on infrared thermography. *Mater. Des.* **2014**, *55*, 785–791. [[CrossRef](#)]
53. Wang, X.; Crupi, V.; Guo, X.; Zhao, Y. Quantitative Thermographic Methodology for fatigue assessment and stress measurement. *Int. J. Fatigue* **2010**, *32*, 1970–1976. [[CrossRef](#)]
54. Williams, P.; Liakat, M.; Khonsari, M.; Kabir, O. A thermographic method for remaining fatigue life prediction of welded joints. *Mater. Des.* **2013**, *51*, 916–923. [[CrossRef](#)]
55. Fan, J.; Guo, X.; Wu, C. A new application of the infrared thermography for fatigue evaluation and damage assessment. *Int. J. Fatigue* **2012**, *44*, 1–7. [[CrossRef](#)]
56. Nowak, M.; Maj, M. Determination of coupled mechanical and thermal fields using 2D digital image correlation and infrared thermography: Numerical procedures and results. *Arch. Civ. Mech. Eng.* **2018**, *18*, 630–644. [[CrossRef](#)]
57. Sharkeev, Y.; Vavilov, V.; Skripnyak, V.A.; Belyavskaya, O.; Legostaeva, E.; Kozulin, A.; Chulkov, A.; Sorokoletov, A.; Skripnyak, V.V.; Eroshenko, A.; et al. Analyzing the Deformation and Fracture of Bioinert Titanium, Zirconium and Niobium Alloys in Different Structural States by the Use of Infrared Thermography. *Metals* **2018**, *8*, 703. [[CrossRef](#)]
58. Sharkeev, Y.P.; Skripnyak, V.A.; Vavilov, V.P.; Legostaeva, E.V.; Kozulin, A.A.; Chulkov, A.O.; Eroshenko, A.Y.; Belyavskaya, O.A.; Glukhov, I.A. Special Aspects of Microstructure, Deformation and Fracture of Bioinert Zirconium and Titanium-Niobium Alloys in Different Structural States. *Russ. Phys. J.* **2018**, *61*, 1718–1725. [[CrossRef](#)]
59. Sharkeev, Y.P.; Vavilov, V.P.; Skripnyak, V.A.; Legostaeva, E.V.; Belyavskaya, O.A.; Kuznetsov, V.P.; Chulkov, A.O.; Kozulin, A.A.; Eroshenko, A.Y.; Zhilyakov, A.Y.; et al. Infrared Thermography and Generation of Heat under Deformation of Bioinert Titanium- and Zirconium-Based Alloys. *Russ. J. Nondestruct. Test.* **2019**, *55*, 533–541. [[CrossRef](#)]
60. Sharkeev, Y.; Vavilov, V.; Skripnyak, V.; Legostaeva, E.; Eroshenko, A.Y.; Belyavskaya, O.; Ustinov, A.; Klopotov, A.; Chulkov, A.; Kozulin, A.; et al. Research on the processes of deformation and failure in coarse- and ultrafine-grain states of Zr1–Nb alloys by digital image correlation and infrared thermography. *Mater. Sci. Eng. A* **2020**, *784*, 139203. [[CrossRef](#)]
61. Legostaeva, E.; Sharkeev, Y.; Eroshenko, A.; Belyavskaya, O.; Vavilov, V.; Skripnyak, V.; Ustinov, A.; Klopotov, A.; Chulkov, A.; Kozulin, A.; et al. Influence of Zr-1 wt.% Nb alloy structure state on its deformation and thermal behavior under quasi-static tension. *Mater. Lett.* **2020**, *285*, 129028. [[CrossRef](#)]
62. Elsayed, F.R.; Hort, N.; Ordorica, M.A.S.; Kainer, K.U. Magnesium Permanent Mold Castings Optimization. *Mater. Sci. Forum* **2011**, *690*, 65–68. [[CrossRef](#)]
63. Nguyen, A.; Kunert, M.; Hort, N.; Schrader, C.; Weisser, J.; Schmidt, J. Cytotoxicity of the Ga-containing coatings on biodegradable magnesium alloys. *Surf. Innov.* **2015**, *3*, 10–19. [[CrossRef](#)]
64. ASTM E1382-97; Standard Test Methods for Determining Average Grain Size Using Semiautomatic and Automatic Image Analysis. ANSI: New York, NY, USA, 2010. [[CrossRef](#)]
65. Park, H.K.; Hong, Y.K.; Lee, S.Q.; Kee, S. Development of a nanoindenter using a piezoelectric actuator. In *Optomechatronic Sensors, Actuators and Control*; SPIE: Philadelphia, PA, USA, 2004; Volume 5602. [[CrossRef](#)]
66. Nie, J.-F. Precipitation and Hardening in Magnesium Alloys. *Metall. Mater. Trans. A* **2012**, *43*, 3891–3939. [[CrossRef](#)]
67. Mengucci, P.; Barucca, G.; Riontino, G.; Lussana, D.; Massazza, M.; Ferragut, R.; Aly, E.H. Structure evolution of a WE43 Mg alloy submitted to different thermal treatments. *Mater. Sci. Eng. A* **2008**, *479*, 37–44. [[CrossRef](#)]
68. Martynenko, N.; Lukyanova, E.; Serebryany, V.; Gorshenkov, M.; Shchetinin, I.; Raab, G.; Dobatkin, S.; Estrin, Y. Increasing strength and ductility of magnesium alloy WE43 by equal-channel angular pressing. *Mater. Sci. Eng. A* **2018**, *712*, 625–629. [[CrossRef](#)]
69. Dobatkin, S.; Galkin, S.; Estrin, Y.; Serebryany, V.; Diez, M.; Martynenko, N.; Lukyanova, E.; Perezhogin, V. Grain refinement, texture, and mechanical properties of a magnesium alloy after radial-shear rolling. *J. Alloys Compd.* **2018**, *774*, 969–979. [[CrossRef](#)]
70. Raynor, G.V. *Physical Metallurgy of Magnesium and Its Alloys*; Pergamon Press: London, UK, 1959; 531p.
71. Zecevic, M.; Beyerlein, I.J.; Knezevic, M. Activity of pyramidal I and II $\langle c+a \rangle$ slip in Mg alloys as revealed by texture development. *J. Mech. Phys. Solids* **2018**, *111*, 290–307. [[CrossRef](#)]

72. Li, J.; Zhang, A.; Pan, H.; Ren, Y.; Zeng, Z.; Huang, Q.; Yang, C.; Ma, L.; Qin, G. Effect of extrusion speed on microstructure and mechanical properties of the Mg-Ca binary alloy. *J. Magnes. Alloy.* **2020**, *9*, 1297–1303. [[CrossRef](#)]
73. Kozulyan, A.A.; Skripnyak, V.A.; Krasnoveikin, V.A.; Skripnyak, V.V.; Karavatskii, A.K. An Investigation of Physico-Mechanical Properties of Ultrafine-Grained Magnesium Alloys Subjected to Severe Plastic Deformation. *Russ. Phys. J.* **2015**, *57*, 1261–1267. [[CrossRef](#)]
74. Glezer, A.M.; Kozlov, E.V.; Koneva, N.A.; Popova, N.A.; Kurzina, I.A. *Plastic Deformation of Nanostructured Materials*; CRC Press: Boca Raton, FL, USA, 2017; 334p. [[CrossRef](#)]
75. Koneva, N.; Kozlov, E.; Trishkina, L.; Pekarskaya, E. Thermodynamics of substructure transformations under plastic deformation of metals and alloys. *Mater. Sci. Eng. A* **1997**, *234–236*, 614–616. [[CrossRef](#)]
76. Hilarov, V.L.; Slutsker, A.I. Description of the thermoelastic effect in solids in a wide temperature range. *Phys. Solid State* **2014**, *56*, 2493–2495. [[CrossRef](#)]
77. Legostaeva, E.; Eroshenko, A.; Vavilov, V.; Skripnyak, V.A.; Chulkov, A.; Kozulin, A.; Skripnyak, V.V.; Glukhov, I.; Sharkeev, Y. Comparative Investigation of the Influence of Ultrafine-Grained State on Deformation and Temperature Behavior and Microstructure Formed during Quasi-Static Tension of Pure Titanium and Ti-45Nb Alloy by Means of Infrared Thermography. *Materials* **2022**, *15*, 8480. [[CrossRef](#)] [[PubMed](#)]
78. Ivanov, A.M.; Lukin, E.S.; Petrova, N.D. Regularities of Deformation and Fracture of Steels Subjected to Equal Channel Angular Pressing and Thermal Processing. *Mater. Sci. Forum* **2008**, *584–586*, 643–648. [[CrossRef](#)]
79. Gadaj, S.; Nowacki, W.; Pieczyska, E. Investigation of temperature distribution during plastic deformation of stainless steel. *Proc. Eurotherm Semin. QIRT* **1996**, *48*, 779–788. [[CrossRef](#)]
80. Taylor, G.I.; Quinney, H. The latent energy remaining in a metal after cold working. *Proc. R. Soc. Lond. Ser. A Contain. Pap. A Math. Phys.* **1934**, *143*, 307–326. [[CrossRef](#)]

Disclaimer/Publisher's Note: The statements, opinions and data contained in all publications are solely those of the individual author(s) and contributor(s) and not of MDPI and/or the editor(s). MDPI and/or the editor(s) disclaim responsibility for any injury to people or property resulting from any ideas, methods, instructions or products referred to in the content.